Efficient nonlinear modelling of spatial flux harmonics of squirrel cage induction motors using inverse flux maps and static FEA

Johannes Stoss, Pierre Mader, Leonard Geier, Akif Karayel, Andreas Liske and Marc Hiller
Institute of Electrical Engineering (ETI)
Karlsruhe Institute of Technology, Karlsruhe, Germany
johannes.stoss@kit.edu

***Abstract*--In this paper a new method for efficient generation of fundamental and harmonic flux maps of squirrel cage induction motors is presented. The maps are generated only by using static finite element analysis in the rotor current reference frame. Thereby, symmetries of the flux linkages are analyzed to further reduce the calculation effort. This enables efficient simulation, real time modelling and control of induction motors including saturation effects and spatial harmonics. This is achieved by using a machine model based on inverse flux mapping.**

***Index Terms*—Induction motors, Nonlinear magnetics, Flux model, harmonics**

I. Introduction

Design of new control algorithms and evaluation over a large variety of operating points require machine models that are computationally efficient but still reflect the behavior in as much detail as possible. This is a particular challenge with induction motors, as it can take several seconds to reach the steady-state operating point after a setpoint change.

Machine models based on inverse flux maps are a possible solution which allow efficient modelling and control of electrical machines [1]. But for these models, initial flux linkage maps must be calculated. In the case of doubly-fed induction motors, high-precision datasets can be generated by applying different current combinations to the two different three phase systems in the stator and rotor [2].

This approach is not possible for induction motors with squirrel-cage rotors, since they have a multi-phase winding system in the rotor instead of three-phase system which can be supplied with specific dq-current combinations.

As the current distribution in the multi-phase system of the squirrel cage is unknown, full identification of the flux maps would require a large variety of extensive transient simulations to cover all operating points for the machine. This approach would be very time consuming, as the settling times of the machine can be large, which causes long evaluation times for each operating point.

This paper proposes a new approach in which a series of static finite element analysis (FEA) simulations is solved time efficiently, allowing fast identification of the multi-dimensional flux maps. In contrast to existing methods [3, 4], the simulations are performed in a rotor current reference frame in order to streamline the simulation setup.

II. Machine Model

The harmonic flux model of the induction machine is based on the known stator voltage equations in the stator oriented αβ-system. The αβ-stator voltages ($v_{\mathrm{S}\alpha}, v_{\mathrm{S}\beta}$) are described as a function of the stator resistance R_{S}, the stator αβ-currents ($i_{\mathrm{S}\alpha}, i_{\mathrm{S}\beta}$) and stator flux linkages ($\psi_{\mathrm{S}\alpha}, \psi_{\mathrm{S}\beta}$).

$$v_{\mathrm{S}\alpha} = R_{\mathrm{S}} \cdot i_{\mathrm{S}\alpha} + \frac{\mathrm{d}\psi_{\mathrm{S}\alpha}}{\mathrm{d}t} \tag{1}$$

$$v_{\mathrm{S}\beta} = R_{\mathrm{S}} \cdot i_{\mathrm{S}\beta} + \frac{\mathrm{d}\psi_{\mathrm{S}\beta}}{\mathrm{d}t} \tag{2}$$

The stator flux linkages are not only dependent on the stator current vector but are also significantly influenced by the rotor position and the rotor currents. Therefore, the currents in the squirrel cage must be modelled.

The squirrel cage has Q_{R} rotor bars per pole pair where

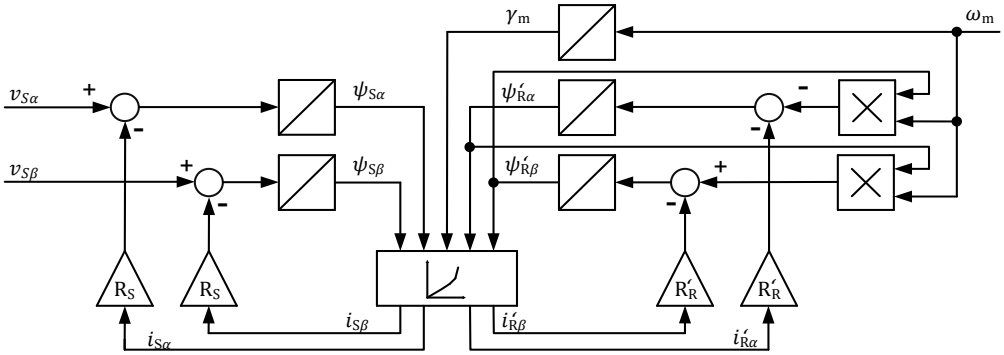

Fig. 1: Flux model of the induction machine

each bar carries its own current $i_{\mathrm{RB},x}\ x \in [1,2,\ldots,Q_\mathrm{R}]$. This results in a Q_R-dimensional rotor current vector for a complete characterization of each operating point.

As this would lead to high model complexity, a simplification must be made for efficient real time modeling. Therefore, it is assumed that, in typical operating points, the fundamental rotor current component is significantly larger than all other components [5]. As this assumption is the foundation for the machine model and FEA setup in this paper it is further analyzed in section III. By using only the fundamental rotor current component, modelling of the rotor can be done by the known rotor voltage equations. In the stator-oriented αβ-reference frame, these consist of the rotor resistance R'_R, the αβ-currents ($i'_{\mathrm{R}\alpha}, i'_{\mathrm{R}\beta}$), the rotor flux linkages ($\psi'_{\mathrm{R}\alpha}, \psi'_{\mathrm{R}\beta}$) and the mechanical rotor frequency ω_m. As the rotor is short-circuited, its voltages are $v_{\mathrm{R}\alpha} = v_{\mathrm{R}\beta} = 0$.

$$v_{\mathrm{R}\alpha} = 0 = R'_\mathrm{R} \cdot i'_{\mathrm{R}\alpha} - \psi'_{\mathrm{R}\beta} \cdot \omega_\mathrm{m} + \frac{\mathrm{d}\psi'_{\mathrm{R}\alpha}}{\mathrm{d}t} \quad (3)$$

$$v_{\mathrm{R}\beta} = 0 = R'_\mathrm{R} \cdot i'_{\mathrm{R}\beta} + \psi'_{\mathrm{R}\alpha} \cdot \omega_\mathrm{m} + \frac{\mathrm{d}\psi'_{\mathrm{R}\beta}}{\mathrm{d}t} \quad (4)$$

The flux linkages are modelled in dependence of the stator and rotor current components in the stator oriented αβ-system. If spatial harmonics are to be modelled the electrical rotor angle γ_m of the rotor is also required. As there is no simple analytical description for the flux linkages, they need to be described as a multi-dimensional mapping f_ψ as shown in chapter IV.

$$f_\psi\colon (i_{\mathrm{S}\alpha}, i_{\mathrm{S}\beta}, i'_{\mathrm{R}\alpha}, i'_{\mathrm{R}\beta}, \gamma_\mathrm{m}) \longmapsto (\psi_{\mathrm{S}\alpha}, \psi_{\mathrm{S}\beta}, \psi'_{\mathrm{R}\alpha}, \psi'_{\mathrm{R}\beta}) \quad (5)$$

Combining stator and rotor equations, the whole system dynamics of the induction machine are modelled with the block diagram shown in fig. 1. This is an adapted form of the general model published in [1] which depends on inverse flux mapping. To run the model, inversion of the flux map (5) has to be performed once in advance by the method described in [1].

As the rotor resistance of the induction machine depends on the operating point, it can also be adjusted accordingly in the model. The change in the rotor resistance is caused by the current displacement in the rotor due to the operating point dependent rotor frequency. Identification of frequency dependent R'_R maps can be achieved by transient locked rotor FEA simulations [6].

III. Spatial Rotor Current Harmonics

The assumption that the rotor current is sinusoidally distributed between the rotor bars is the foundation for the machine model and FEA setup in this work. Even though this assumption is reported to only cause negligible error in [3, 4], the real rotor current distribution is analyzed further using transient FEAs. All FEAs were performed with the machine data given in table I and the design shown fig. 2. Stator and rotor are not skewed. This favors the formation of current harmonics therefore this model presents a worst-case scenario.

TABLE I
Basic Machine Geometry Data

Symbol	Meaning	value
p	Number of pole pairs	**2**
N	Stator slot number	**36**
Q_R	Rotor bars per pole pair	**14**
d_R	Rotor diameter	**160 mm**
δ_R	Airgap	**0.75 mm**

To analyze the rotor current harmonics, the FEA model was operated with a constant voltage amplitude at a supply frequency of 50 Hz. This is similar to grid or inverter operation at a stationary operating point.

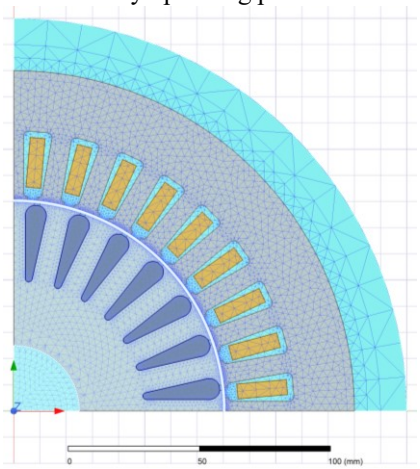

Fig. 2: Machine design and mesh grid used for FEA simulation.

Fig.3 shows the resulting rotor bar currents at 0.51 Hz rotor frequency at stationary operation. This is equivalent to $i_\mathrm{d} = 26.4$ A and $i_\mathrm{q} = 26.8$ A in the rotor flux reference frame. The current distribution along the rotor bar position shows a strong fundamental component, but harmonics are also present. Since a strictly sinusoidal current distribution is assumed in the model, the model error increases as the amount of harmonics rise. Therefore, the total harmonic distortion (THD) of the spatial rotor current distribution is used for evaluation. The average THD value for the data of fig. 3 is -28.83 dB.

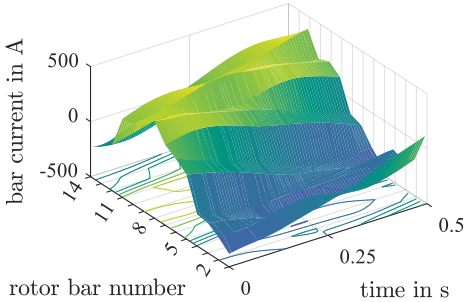

Fig. 3: Rotor bar currents during transient FEA simulation.

In addition to analyzing the current THD, the rotor current distribution can also be analyzed using the rotor-oriented $\alpha\beta_\mathrm{R}$-system. This can be seen as a spatial Fourier transform along the rotor circumference. Therefore, the

Q_R -dimensional current vector shown in fig. 3 is transformed to the $\alpha\beta_R$-system using $\underline{b} = e^{j\cdot 2\pi/Q_R}$ according to [7].

$$\begin{bmatrix} \underline{i}_{R\alpha\beta_R,1} \\ \underline{i}_{R\alpha\beta_R,2} \\ \vdots \\ \underline{i}_{R\alpha\beta_R,Q_R} \end{bmatrix} = \begin{bmatrix} 1 & 1 & \dots & 1 \\ 1 & \underline{b} & \cdots & \underline{b}^{Q_R-1} \\ \vdots & \vdots & \ddots & \vdots \\ 1 & \underline{b}^{Q_R-1} & \dots & \underline{b}^{(Q_R-1)^2} \end{bmatrix} \cdot \begin{bmatrix} i_{RB,1} \\ i_{RB,2} \\ \vdots \\ i_{RB,Q_R} \end{bmatrix} \quad (6)$$

It should be noted that this transformation does not preserve the amplitude, meaning the real current amplitude of each component is Q_R-times lower than the amplitude of $\underline{i}_{R\alpha\beta_R,x}$. The transformation leads to Q_R complex current components, of which the second half is conjugate complex to the first half. The DC component is given by $\underline{i}_{R\alpha\beta_R,1}$. Fig. 4 shows the results of the transform being applied to the data shown in fig. 3. The 2nd, fundamental component, is significantly larger than all other components, confirming the assumptions made in section II. The DC component, given by index 1 is zero. This is expected, as a squirrel cage rotor doesn't allow a DC current component due to its wiring connection. In addition, the 2nd and 4th harmonic of the fundamental rotor current component, given by index 4 and 6, are present. As the induction motor is modeled symmetrically in the FEA, components 3, 5 and 7 also become zero.

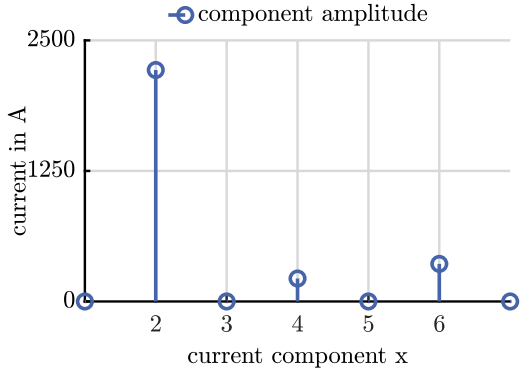

Fig. 4: Averaged amplitudes mean$\{|\underline{i}_{R\alpha\beta_R,x}|\}$ over the time interval shown in fig. 3.

As the model needs to be valid for the whole operating range, the rotor current distribution is analyzed for several operating points using transient FEA simulations. Postprocessing and data analysis were performed equal to the shown operating point of fig. 3. To provide a clear conclusion about the occurrence of current harmonics in the rotor, the THD was evaluated for each operating point. The stator frequency was set constant to 25 Hz. The stator voltage amplitude and rotor speed were adapted for each operating point. The results in fig. 5 are given in the rotor flux reference frame, as it is widely used for control and modelling for induction machines.

Fig. 5 gives the spatial rotor current THD for different operating points in rotor flux orientation. As the stator frequency differs from the previously shown the operating point, a slight deviation is expected. For most operating points, the THD is larger than -20 dB resulting in a damping ratio greater 10 for the harmonic components compared to the fundamental. As there is no rotor current at stationary operation for $i_{Sq} = 0$ A, those areas have been interpolated.

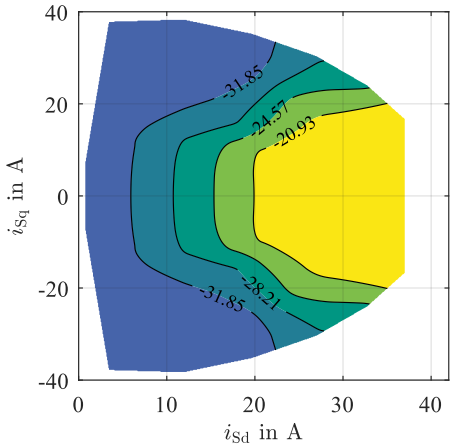

Fig. 5: Rotor current THD in dB at transient FEA.

For further evaluation, the sum of the rotor current harmonics is given in fig. 6. It shows roughly proportional behavior to the stator current amplitude. Therefore, the relative error of the stator currents caused by neglecting the rotor current harmonics can be assumed to be almost constant over the entire operating range.

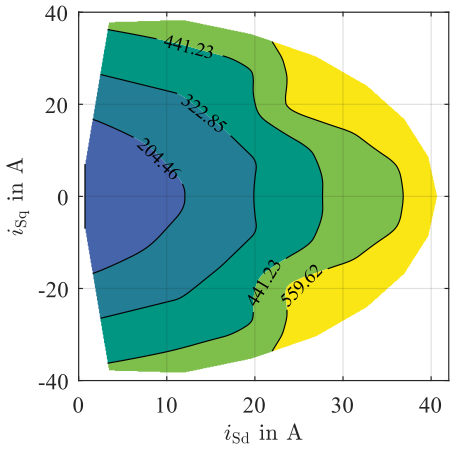

Fig. 6: Sum of averaged rotor current amplitudes mean$\{|\underline{i}_{R\alpha\beta_R,x}|\}$ $x \in [3,4,\dots,Q_R]$ at transient FEA.

The results of this section confirm the assumption of a dominant sinusoidal current distribution in the rotor bars. This was proved by transient FEA simulations over wide range of operating points, even if the rotor is not skewed. But the data also shows harmonic components at all operating points which inevitably lead to model errors. By analyzing the harmonic content, their impact on the output currents can assumed to be almost constant. As further demonstrated in the validation results in chapter VI, the overall model errors are mostly negligible.

IV. Generation of Flux Maps

As the model shown in fig. 1 requires detailed flux maps f_ψ, they need to be acquired in advance by FEA

simulations or measurements [8, 9]. To make this process as efficient as possible, a series of static FEA simulations are performed instead of transient simulation. This significantly reduces the computation effort for each operating point. Using the simplifications of the rotor current distribution made in chapter II and III, the operating points of the static FEA simulation can be defined very conveniently.

A. General FEA setup

The setup of the static FEA is performed in rotor current orientation instead of stator orientation, as it streamlines the setup through the simplified geometry relationship. This results in a similar simulation grid and flux maps as for electronically excited synchronous machines that are shown in [1].

Fig. 7 shows the different reference systems used for simulation and modelling. The rotor flux reference frame is not shown, as it is exclusively used for evaluation of the results in chapter IV.

The stator-fixed αβ-system is thereby only required for generation of the flux maps of the presented model in fig. 1. The FEA setup is performed in rotor current orientation defined by the $\mathrm{dq_{iR}}$-system shown in fig. 7. The current space vector $\underline{i}_\mathrm{R}$ represents the fundamental amplitude of the spatial sinusoidal current distribution in the rotor bars.

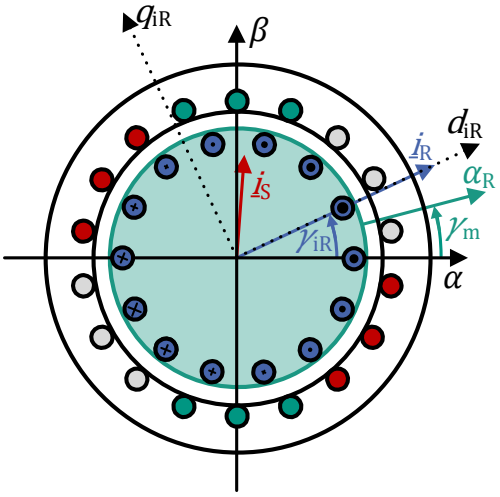

Fig. 7: Coordinate systems and angle definitions. '·' and 'x' indicate rotor current amplitude and direction.

The angle γ_iR is the angular shift between the stator-fixed αβ-system and the $\mathrm{dq_{iR}}$-system in rotor current orientation. γ_m is the angle between the rotor fixed $\alpha\beta_\mathrm{R}$-system and the stator-fixed αβ-system. It defines the relative position of the rotor bars to the slots and windings in the stator. The current space vector $\underline{i}_\mathrm{S}$ describes the stator current distribution relative to the rotor current space vector represented by the $\mathrm{dq_{iR}}$-system.

Fig. 8 shows the simulation grid (red) for the stator current space vector $\underline{i}_\mathrm{S}$ that is required for each set of $\underline{i}_\mathrm{R}$, γ_iR and γ_m. This means, that for each of these current combinations, different rotor d-currents need to be applied while rotating the coordinate system to evaluate the flux harmonics impressed by the stator windings and geometry. Furthermore, the rotor position needs to be varied to take the rotor angle dependent harmonics into account.

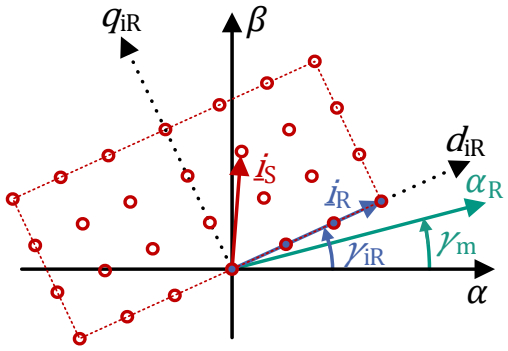

Fig. 8: Stator current grid for static FEA simulation for a defined rotor angle and rotor current.

Table II shows the parameters used to set up the static FEA according to the procedure presented. The results are shown in chapter V. All values are thereby given in stator related quantities.

TABLE II
SIMULATION SETUP IN ROTOR CURRENT ORIENTATION

Symbol	min	max	increment
i_Sd	-60 A	60 A	7.5 A
i_Sq	-60 A	60 A	7.5 A
i'_Rd	0 A	60 A	7.5 A
γ_iR	0°	$60° - 20°/7$	$20°/7$
γ_m	0°	$180°/7 - 20°/7$	$20°/7$

B. Symmetries

Utilizing symmetries is a common way to reduce computation effort on a FEA. Depending on evaluation of the fundamental component or the harmonics, different symmetries can be utilized.

In addition to that, skewing can also be applied in postprocessing, further reducing the computation effort compared to a multi slice FEA [3]. Methods for continuous skewing during postprocessing are presented in [3, 4].

1) Fundamental flux maps

For the fundamental component of the flux maps, the symmetries are equivalent to the ones of the electronically excited synchronous machine. Therefore, the stator and rotor d-flux linkages for negative stator q-currents can be calculated using the axial symmetry of the flux maps with $x \in \{\mathrm{Sd}, \mathrm{Rd}\}$.

$$\psi_x(i_\mathrm{Sd}, -i_\mathrm{Sq}, i_\mathrm{Rd}) = \psi_x(i_\mathrm{Sd}, i_\mathrm{Sq}, i_\mathrm{Rd}) \tag{7}$$

As for the q-flux linkages, extension is performed by applying the point symmetry for $x \in \{\mathrm{Sq}, \mathrm{Rq}\}$.

$$\psi_x(i_\mathrm{Sd}, -i_\mathrm{Sq}, i_\mathrm{Rd}) = -\psi_x(i_\mathrm{Sd}, i_\mathrm{Sq}, i_\mathrm{Rd}) \tag{8}$$

2) Harmonic flux maps

To further reduce the computation effort for the harmonic flux maps, angular symmetries can also be

utilized by analyzing the periodicities of the maps. Therefore, the isolated periodicities of the stator and the rotor are analyzed first.

For the rotor harmonics, $\Delta\gamma_{\mathrm{m,per}}$ is defined as the periodicity along the γ_{m} -axis. It is caused by the distribution of the rotor bars along the rotor circumference. This means that shifting the rotor angle γ_{m} one rotor bar division while keeping γ_{iR} and the rotor current amplitude constant, results in the same flux linkages. Therefore, $\Delta\gamma_{\mathrm{m,per}}$ is chosen to $360°/Q_{\mathrm{R}}$ reducing the range of γ_{iR} in the FEA to the interval of $[0°, 360°/Q_{\mathrm{R}}]$.

Similar to synchronous machines, a symmetry of $\Delta\gamma_{\mathrm{iR,per}} = 60°$ for the stator flux linkage harmonics can be observed. This reduces the range of γ_{iR} in the FEA setup to the interval of $[0°, 60°]$. Both symmetries are also reflected in the simulation setup given in table II.

When superimposing these individual periodicities for extension of the flux maps, it is necessary to consider the interaction between rotor and stator geometries. This means that a simple shift of the flux maps along the γ_{iR}-axis by $\Delta\gamma_{\mathrm{iR,per}}$ is not sufficient as it does not cover the harmonic components caused by the rotor geometry. Therefore, a further shift of $\Delta\gamma_{\mathrm{m}}$ to the rotor angle γ_{m} is applied to establish the same magnetic path. The shifting angle $\Delta\gamma_{\mathrm{m}}$ depends on the previously determined isolated periodicities.

$$\Delta\gamma_m = \Delta\gamma_{iR,per} \bmod\left(\Delta\gamma_{m,per}\right) \tag{9}$$

Using the calculated shifting angles the harmonic flux map can be extended along the γ_{iR}-axis for a fixed set of $i_{\mathrm{Sd}}, i_{\mathrm{Sq}}$ and i_{Rd} with $x \in \{\mathrm{Sd}, \mathrm{Sq}, \mathrm{Rd}, \mathrm{Rq}\}$ as follows:

$$\psi_x(\gamma_{iR} + \Delta\gamma_{iR,per}, \gamma_m) = \psi_x(\gamma_{iR}, \gamma_m + \Delta\gamma_m) \tag{10}$$

Along the γ_{m}-axis no additional shifting needs to be applied. Therefore, extension can be performed by:

$$\psi_x(\gamma_{iR}, \gamma_m + \Delta\gamma_{m,per}) = \psi_x(\gamma_{iR}, \gamma_m) \tag{11}$$

Fig. 9 shows the area which needs to be identified by FEA (blue). The full flux map (gray) is generated by the described periodic extension, which needs to be performed for each fixed set of $i_{\mathrm{Sd}}, i_{\mathrm{Sq}}$ and i_{Rd}.

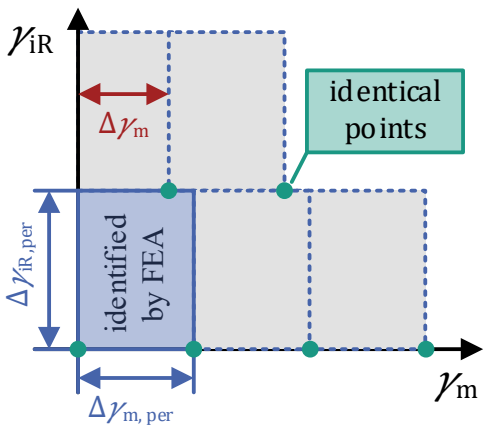

Fig. 9: Extension of the harmonic flux maps

Subsequently, extension for negative q-currents can be performed as well. By taking the angular dependencies into account, the extension of the rotor and stator d-flux linkages maps are adapted with $x \in \{\mathrm{Sd}, \mathrm{Rd}\}$ as follows.

$$\psi_x(i_{\mathrm{Sd}}, -i_{\mathrm{Sq}}, i_{\mathrm{Rd}}, \gamma_{iR}, \gamma_m) = \psi_x(i_{\mathrm{Sd}}, i_{\mathrm{Sq}}, i_{\mathrm{Rd}}, -\gamma_{iR}, -\gamma_m) \tag{12}$$

Like the d-components, the extension of the q-flux linkage maps is performed by adapting eqn. (8) to include the angular dependencies. This results for $x \in \{\mathrm{Sq}, \mathrm{Rq}\}$ in:

$$\psi_x(i_{\mathrm{Sd}}, -i_{\mathrm{Sq}}, i_{\mathrm{Rd}}, \gamma_{iR}, \gamma_m) = -\psi_x(i_{\mathrm{Sd}}, i_{\mathrm{Sq}}, i_{\mathrm{Rd}}, -\gamma_{iR}, -\gamma_m) \tag{13}$$

C. *Conversion of the flux maps*

The FEA simulation results in rotor and stator related data. As the flux model shown in fig.1 requires stator related data, conversion of the rotor quantities to the stator side is necessary. This is performed based on the transformers equivalent circuit using the effective winding numbers [10]. The transformation factors for current k_{i} and voltage k_{v} are defined first, with m_{S} being the number of strings, w_{S} the number of windings and ξ_S the winding factor of the stator. ξ_S is thereby analytically determined according to [10].

$$k_i = \frac{2 \cdot m_S \cdot w_S \cdot \xi_S}{Q_R} \tag{14}$$

$$k_v = 2 \cdot w_S \cdot \xi_S \tag{15}$$

It is therefore assumed that the squirrel cage rotor has 0,5 turns and a winding factor of 1. The parameters are then transformed to the stator side by:

$$\psi'_{Rd} = \psi_{Rd} \cdot k_v \tag{16}$$

$$i'_{Rd} = \frac{i_{Rd}}{k_i} \tag{17}$$

$$R'_R = R_R \cdot k_v \cdot k_i \tag{18}$$

Furthermore, transformation of rotor current orientation to the stator fixed αβ-orientation and inversion of the flux map is performed as shown in [1].

V. Simulation Results

The flux maps in this chapter were generated using the FEA setup given in table II. Subsequently, the maps were extended using the symmetries presented to generate a full, angle-dependent flux map. This result is a 5-dimensional flux map as described in eq. (5). To allow presentation of the data, a dimensionality reduction was conducted for the plots. Therefore, the fundamental flux linkages are shown first neglecting all harmonic components. Second, the angular dependencies of the flux linkages for a defined stator- and rotor current are presented.

A. *Fundamental flux maps*

Fig. 10 shows the stator flux maps. The rotor and stator flux linkage maps only differ slightly due to stray flux. As

the differences are barely visible, they are not shown separately in this paper. The fundamental flux maps are generated by averaging the results of the FEA simulation across all rotor angles and all rotor current angles.

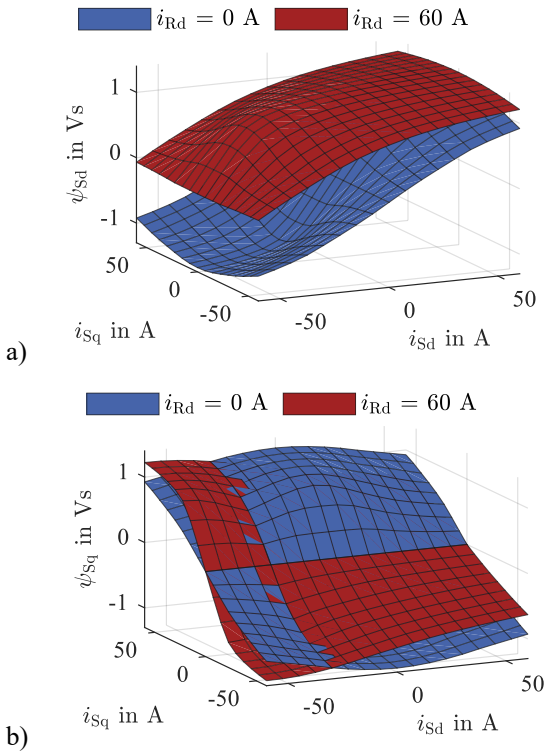

Fig. 10: Fundamental stator flux linkages maps of ψ_{Sd} in a) and ψ_{Sq} in b) in rotor current orientation at different rotor currents.

As expected, the maps shown in fig. 10 have a similar shape as the electrically excited synchronous machine [1, 11]. For use in the flux model, the data needs to be transformed into stator orientation and inverted. The full inverse flux map has a size of approximately 70MB.

B. Harmonic flux maps

For evaluation of the spatial harmonics, no averaging is applied. The data is extended for the rotor angle and rotor current angle using the symmetries given in chapter IV.

Fig. 11 shows the harmonic flux maps for the operating point of $i_{Sd} = 15\,A$, $i_{Sq} = 30\,A$ and $i'_{Rd} = 30\,A$ in dependence of the rotor current angle γ_{iR} and the rotor angle γ_m. Thereby, the periodicities presented in chapter IV can be observed. The 14 rotor bars per electrical period lead to a 14th order harmonic visible along the axis of γ_m. The stator is dominated by its typical harmonics which are to be seen as a multiple of the 6th order along the γ_{iR} axis. As both components affect each other, this results in a 2-dimensional map for the spatial harmonics, leading to a overall 5-dimensional flux map for all current and angle components.

For use in the flux model, the data was also transformed into stator orientation and inverted. The full inverse flux map has a size of approximately 980MB. For real-time operation the resolution can be further decreased without drastically reducing the model quality.

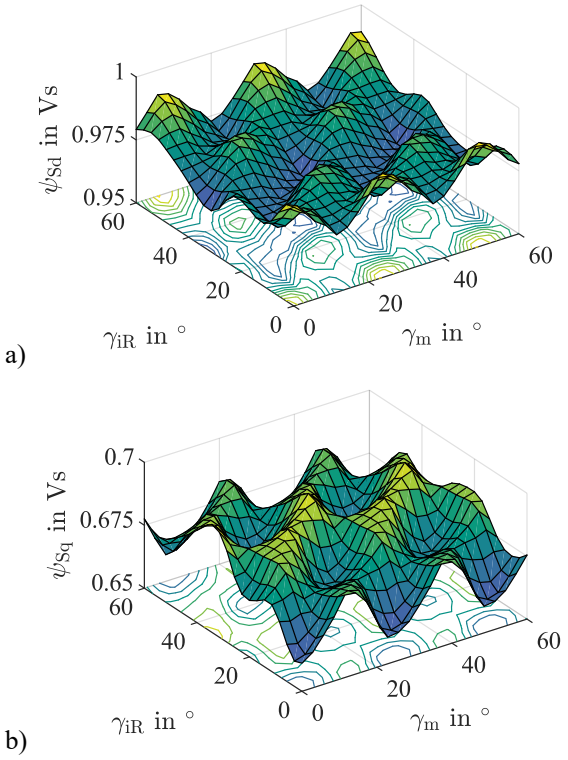

Fig. 11: Harmonic flux maps of ψ_{Sd} in a) and ψ_{Sq} in b) in rotor current orientation for $i_{Sd} = 15\,A$, $i_{Sq} = 30\,A$ and $i'_{Rd} = 30\,A$.

VI. Validation

The machine model is validated using voltage excitation as it differs from the current excitation used in the static FEA. Validation is only performed for the harmonic model, as it is the most challenging system. The results are first shown for transient operations followed by stationary operation.

The presented flux model was built in MATLAB Simulink® using the flux maps presented in chapter V in inverted form. For comparison a transient simulation of the machine was performed in Ansys Maxwell® using a step size of 100 µs. No skewing was applied to the stator or rotor. Each model was supplied by identical ideal voltage sources at a defined rotational speed.

To allow an unbiased evaluation of the results, the data is shown in the rotor flux reference frame as it is typically used for control of induction machines. It should be noted that the data in the previous chapters was presented in the rotor current reference frame, therefore it cannot be directly transferred to the presented validation results in this chapter.

A. Transient performance

The harmonic model is first shown during a transient operation. The input variables are shown in fig. 12. The rotor speed was changed from 0 rpm to 744 rpm, resulting in a rotor frequency of 0.2 Hz at $t = 0.25\,s$. The frequency of the three-phase stator voltage was kept constant at 25 Hz. The voltage amplitude was increased from 0 V to 62.5 V according to fig. 11.

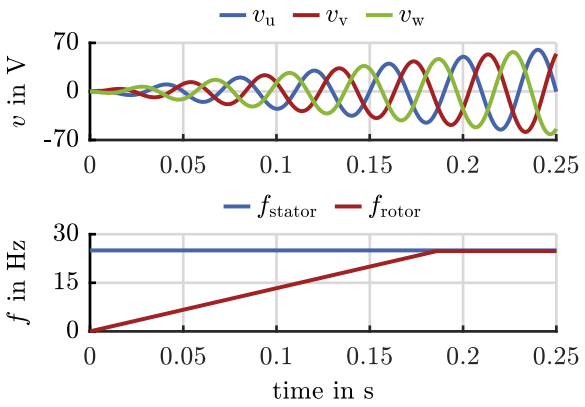

Fig. 12: Phase voltages and frequencies of stator and rotor during startup shown in fig. 13 and fig. 14.

Fig. 13 shows the resulting stator currents. The data of the presented model are indicated by the index SIM. Although the operating point is continuously changed during the simulation, the stator currents are accurately modelled.

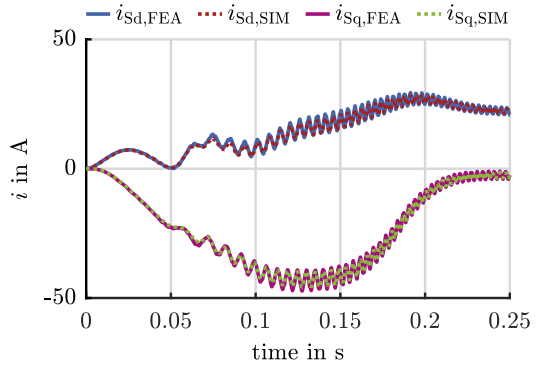

Fig. 13: Comparison of the machine model stator currents with transient FEA at startup.

The stator flux linkages for both models are given in fig. 14. Due to the increasing supply voltage amplitude, the stator flux linkages are also rising. The presented simulation model can thereby reproduce the whole transient behavior of the machine to a high degree. This makes the model also suitable for parameterizing and testing dynamic machine control algorithms.

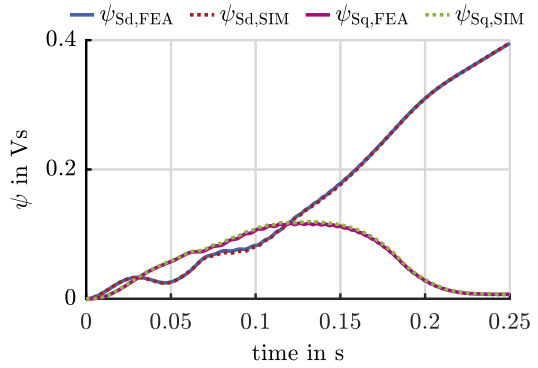

Fig. 14: Comparison of the machine model stator flux linkages with transient FEA at startup.

B. *Stationary performance*

For the evaluation of the stationary performance, both models were supplied with a constant voltage amplitude of 325 V at 51.1 Hz. The rotational speed was kept constant at 1517 rpm resulting in a rotor frequency of 0.53 Hz.

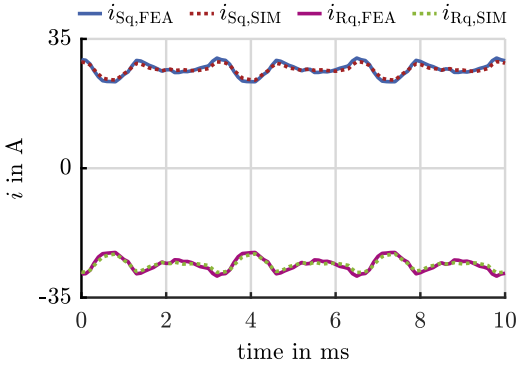

Fig. 15: Comparison of the machine model rotor and stator q-currents with transient FEA at constant voltage amplitude.

As the currents remained constant, during computation of the flux maps, the angular dependency of the magnetic path resulted in harmonics of the flux linkage maps. Here, the voltage amplitude is chosen constant. As shown in fig. 15, the angular dependencies are thus reflected by the currents. Despite the neglection of the additional rotor current components the current harmonics are precisely mapped by the model.

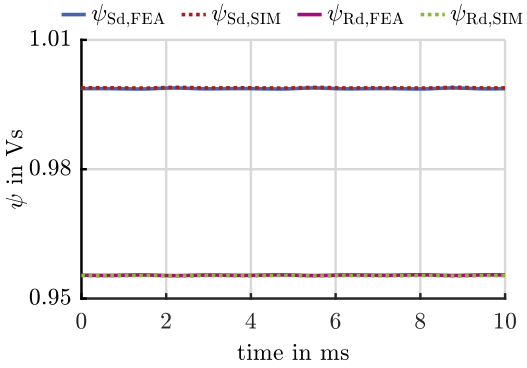

Fig. 16: Comparison of the machine model rotor and stator d-flux linkages with transient FEA at constant voltage amplitude.

Fig. 16. shows the stator and rotor d-flux linkage. Since the stator is supplied with constant voltage, almost no flux harmonics are expected. This is also reflected by both models. The results further demonstrate that the stray flux, which is represented by the deviation of stator and rotor flux linkage, is covered by both models identically.

For a better evaluation of the overall accuracy of the model, the error of the stator currents has been evaluated for different operating points. Therefore, the relative error of the stator currents at stationary operation was calculated as shown in eqn. (19). The results were averaged for a time interval of 0.3 s for each operating point.

$$\Delta i_{\%} = \frac{\mathrm{mean}\{|\underline{i}_{S,\mathrm{FEA}} - \underline{i}_{S,\mathrm{SIM}}|\}}{\mathrm{mean}\{|\underline{i}_{S,\mathrm{FEA}}|\}} \cdot 100\% \qquad (19)$$

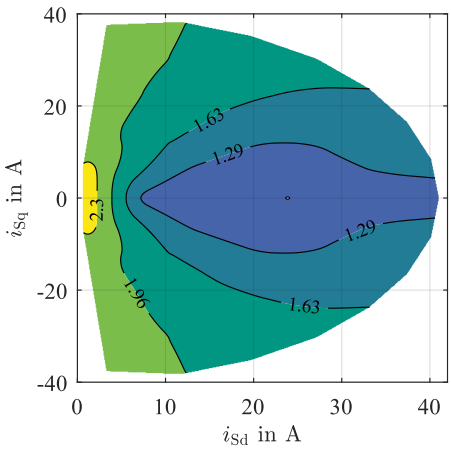

Fig. 17: Relative error in $\Delta i_{\%}$ of the stator currents at different operating points compared to FEA.

Fig. 17 shows the model error $\Delta i_{\%}$. For almost all operating points it is below 2 %. The presented model error $\Delta i_{\%}$ is thereby a combination of various causes:

- Neglection of the rotor current harmonics as shown in chapter III
- Neglection of the frequency dependence of the model resistances
- Numerical errors caused by transformation, interpolation and inversion of the flux map
- Different mesh grids for transient and static FEA

VII. Conclusion

This paper presents a new technique, that allows efficient simulation and modelling of the fundamental machine behavior as well es the spatial harmonics of squirrel cage induction machines. Using the presented model in MATLAB Simulink reduces the simulation time by a factor of 20,000 compared to transient FEA simulation in Ansys Maxwell. This allows to tune controllers more efficiently for transient behavior and harmonics.

The model data is thereby generated only using static FEA simulations to reduce the computational effort. Further reduction was achieved by utilizing the symmetries of the machine and flux maps. Furthermore, the simulation procedure, postprocessing and modelling technique was validated by several transient FEA simulations. It shows a good alignment of the results for the given machine design.

In comparison to known methods for modelling of doubly-fed induction motors, the model lookup table size could be reduced in this paper due to improved memory utilization by a factor of eight while even modelling a more complex system at high precision [1, 2].

As only one machine geometry was examined in this paper, no conclusions can be drawn to the general validity and transferability of the shown methods. For evaluation of new machine designs, the shown spatial current distribution and harmonics analysis can give a clear and fast indication of the transferability to a new design.

VIII. References

[1] Leonard Geier, Johannes Stoss, Andreas Liske, and Marc Hiller, "Generalized Inversion of n-dimensional Flux Maps for Unified Nonlinear Machine Models and Predictive Control Algorithms," *2023 IEEE Energy Conversion Congress*.

[2] P. Peng and P. Han, "Generalized High-Fidelity Reduced-Order Modeling of Doubly-Fed Machines and Induction Machines," in *2022 IEEE Energy Conversion Congress and Exposition (ECCE)*, Detroit, MI, USA, Oct. 2022 - Oct. 2022, pp. 1–8.

[3] J.-H. Lee, Y.-C. Kwon, and S.-K. Sul, "High-Fidelity Induction Motor Simulation Model Based on Finite Element Analysis," *IEEE Trans. Ind. Electron.*, vol. 69, no. 10, pp. 9872–9883, 2022, doi: 10.1109/TIE.2022.3163556.

[4] M. Carbonieri and N. Bianchi, "A Complete and Fast Analysis Procedure for Three-Phase Induction Motors Using Finite Element, Considering Skewing and Iron Losses," *Applied Sciences*, vol. 11, no. 5, p. 2428, 2021, doi: 10.3390/app11052428.

[5] A. R. Munoz and T. A. Lipo, "Complex vector model of the squirrel-cage induction machine including instantaneous rotor bar currents," *IEEE Trans. on Ind. Applicat.*, vol. 35, no. 6, pp. 1332–1340, 1999, doi: 10.1109/28.806047.

[6] M. Carbonieri, N. Bianchi, and L. Alberti, "Direct Analysis of Induction Motor Using Finite Element," in *2018 IEEE Energy Conversion Congress and Exposition (ECCE)*, Portland, OR, USA, 2018, pp. 277–283.

[7] White, David Calvin, Woodson, Herbert H., *Electromechanical energy conversion*. New York: Wiley, 1959.

[8] Johannes Stoss, Akif Karayel, Leonard Geier, Andreas Liske, Marc Hiller, "Identification of rotor and stator flux linkage maps of squirrel cage induction motors based on identification of rotor time constant maps," *2023 25rd European Conference 2023*, vol. 2023.

[9] J. Kullick and C. M. Hackl, "Nonlinear Modeling, Identification, and Optimal Feedforward Torque Control of Induction Machines Using Steady-State Machine Maps," *IEEE Trans. Ind. Electron.*, vol. 70, no. 1, pp. 211–221, 2023, doi: 10.1109/TIE.2022.3153811.

[10] A. Binder, *Elektrische Maschinen und Antriebe: Grundlagen, Betriebsverhalten,* 2nd ed. Berlin, Heidelberg: Springer Berlin Heidelberg, 2018.

[11] Patrick Winzer, Jan Richter, and Martin Doppelbauer, "Dynamic Control of Generalized Electrically Excited Synchronous Machines Using Predictive Flux Control," 2016.